Mapping geological structures in bedrock via large-scale direct current resistivity and time-domain induced polarization tomography

Rossi, Matteo; Olsson, Per Ivar; Johanson, Sara; Fiandaca, Gianluca; Bergdahl, Daniel Preis; Dahlin, Torleif

Published in:
Near Surface Geophysics

DOI:
10.3997/1873-0604.2017058

2017

Document Version:
Version created as part of publication process; publisher's layout; not normally made publicly available

Near Surface Geophysics, 2017, **15**, 657-667 doi: 10.3997/1873-0604.2017058

Mapping geological structures in bedrock via large-scale direct current resistivity and time-domain induced polarization tomography

Matteo Rossi[1*], Per-Ivar Olsson[1], Sara Johanson[1], Gianluca Fiandaca[2], Daniel Preis Bergdahl[3] and Torleif Dahlin[1]

[1] *Division of Engineering Geology, Lund University, Box 118, 221 00 Lund, Sweden*
[2] *HydroGeophysics Group, Department of Geoscience, Aarhus University, 8000 Aarhus, Denmark*
[3] *Department of Geology, Lund University, Box 118, 221 00 Lund, Sweden*

Received August 2017, revision accepted November 2017

ABSTRACT

An investigation of geological conditions is always a key point for planning infrastructure constructions. Bedrock surface and rock quality must be estimated carefully in the designing process of infrastructures. A large direct-current resistivity and time-domain induced-polarization survey has been performed in Dalby, Lund Municipality, southern Sweden, with the aim of mapping lithological variations in bedrock. The geology at the site is characterised by Precambrian granitic gneisses and amphibolites, which are intensely deformed, fractured, and partly weathered. In addition, there are northwest-trending Permian dolerite dykes that are less deformed.

Four 2D direct-current resistivity and time-domain induced-polarization profiles of about 1-km length have been carefully pre-processed to retrieve time-domain induced polarization responses and inverted to obtain the direct-current resistivity distribution of the subsoil and the phase of the complex conductivity using a constant-phase angle model. The joint interpretation of electrical resistivity and induced-polarization models leads to a better understanding of complex three-dimensional subsoil geometries. The results have been validated by lithological descriptions from several drillings. In addition, direct-current resistivity and time-domain induced-polarization logging has been carried out in two different boreholes, showing a good match with the results of the surface direct-current resistivity and time-domain induced-polarization profiles.

The direct-current resistivity and time-domain induced-polarization methodology proved to be a suitable technique for extensively mapping weathered zones with poor geotechnical characteristics and tectonic structures, which can lead to severe problems for infrastructure construction and/or constitute risk zones for aquifer contamination.

INTRODUCTION

Knowledge of geological conditions is needed in order to plan infrastructure construction work of, for example, building foundations or underground facilities and tunnels. The level of desired knowledge varies between projects and ranges from simple estimations of bedrock surface topography to detailed estimations of rock quality in terms of stability and hydraulic properties (CEN 2004). Identification of highly permeable zones is also critical from a groundwater resources management and environmental risk assessment point of view, as they control the behaviour of the flow system.

In order to provide spatially resolved variation of rock quality, the electrical resistivity tomography (ERT) method has been successfully employed in many field cases. During the construction of the Hallandsås Tunnel in southern Sweden, for example, the ERT profiles could predict challenging zones with highly fractured water-bearing or weathered unstable rock (Dahlin, Bjelm and Svensson 1999; Danielsen and Dahlin 2009). Similarly, fractured zones in bedrock have been detected with ERT in several other field cases, e.g., tunnel projects in Italy (Cavinato *et al.* 2006) and Norway (Ganerød *et al.* 2006; Rønning *et al*. 2014). A large-scale application of ERT to investigate bedrock geology is shown by Storz, Storz and Jacobs (2000), where the authors detected electrically conductive fault zones in the metamorphic crystalline basement.

* matteo.rossi@tg.lth.se

The induced polarization (IP) mechanism can be described as a charge-up effect, which can be measured simultaneously with direct-current (DC) resistivity in time-domain ERT surveys. Clay weathering in bedrock fractures has been shown to give rise to anomalies in IP, which makes these features distinguishable from non-weathered fractures (e.g., Marescot, Monnet and Chapellier 2008; Magnusson, Fernlund and Dahlin 2010). It is also well known that certain conductive minerals, e.g., sulphide minerals, give rise to large IP anomalies (e.g., Pelton *et al.* 1978). The combination of resistivity and IP measurements can therefore give complementary information on different physical aspects of the investigated bedrock.

A DC resistivity and time-domain induced polarization (DCIP) survey was carried out along four lines at Dalby, Lund Municipality, southern Sweden. The purpose of the survey was to map lithological variations in bedrock as part of site investigations for a planned underground facility. The site is located in the tectonic structure known as Tornquist Zone (TZ), and the bedrock at the site consists of a complex and deformed stratigraphy of mainly granitic gneiss, amphibolite, and dolerite dykes. A large quarry, located immediately north of the investigated area, gives an excellent overview of the geological conditions that can be expected.

In this study, we aim at refining the characterisation of the bedrock by integrating resistivity and IP using recently developed data acquisition, processing, and inversion techniques (Fiandaca *et al.* 2012; Olsson *et al.* 2015; Olsson *et al.* 2016). The refined subsoil characterisation can potentially lead to a better description and understanding of bedrock materials, their quality, and geometrical distribution.

GEOLOGICAL SETTING

Regional geology

The crystalline basement in southern Sweden mainly consists of granitoid rocks in the western part and metamorphosed rocks with associated mafic intrusions in the eastern part (Figure 1). The giant felsic magmatic intrusions are part of the Transscandinavian Igneous Belt (TIB) dated at ca. 1.85–1.67 Ga (Högdahl *et al.* 2004). The TIB has been subsequently deformed and metamorphosed during both compressional and extensional events. The Hallandian orogeny was a compressional event, which occurred around 1.45 Ga ago when the Baltica tectonic plate presumably collided with an unknown southern continent (e.g., Hubbard 1975; Brander and Söderlund 2009). A second orogenic event, known as the Sveconorwegian orogeny (e.g., Johansson, Lindh and Möller 1991; Wahlgren, Cruden and Stephens 1994; Möller *et al.* 2002) occurred at 1.1–0.9 Ga.

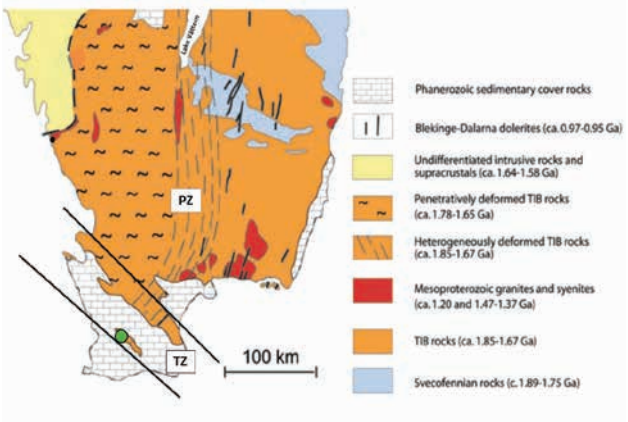

Figure 1 Simplified geological map of southern Sweden. Solid black lines delineate the northern part of the horst–graben system known as TZ. The grey dashed lines highlight the PZ. The green dot is the location of the study area in Dalby (modified from Söderlund *et al.* 2008).

The Protogine Zone (PZ) in south-central Sweden can be defined as a boundary of the deformation and metamorphism attributed to the Sveconorwegian orogeny; it is a lithological limit between the western gneisses and the almost unmetamorphosed eastern granites. The PZ is a structural zone, mainly elongated N–S, ca. 25–30 km wide, south of Lake Vättern. It is pervasively deformed with a variety of strike–parallel geological features: shear and fault zones (Wahlgren *et al.* 1994); several generations of dolerite dykes (Söderlund and Ask 2006); and mineralisation in hydrothermal systems under low-pressure conditions (Geisler and Schleicher 2000). The intrusions along the PZ have undergone various degrees of re-working and deformation.

The second prominent structural zone in southern Sweden is the horst–graben system of the TZ, a system of generally NW–SE trending faults and shear zones that cross Europe from the North Sea to the Black Sea. It has been active from ca. 300 Ma ago with alternating stages of compression and extension resulting in faulting and intrusion of fracture-parallel diabase dykes dated ca. 280 Ma (Klingspor 1976). The horsts consist of Precambrian gneisses and amphibolites, whereas in the grabens, Palaeozoic era sedimentary rocks cover the crystalline basement.

Study area

The study area is situated in the municipality of Lund (southern Sweden), southwest of the Dalby quarry (Figure 2). A geological survey at the quarry, where there is extensive exposure of the bedrock, gives a preview of the expected lithological setting in the area investigated by geophysical surveying (Figure 3).

The crystalline basement consists mainly of granitic gneiss, which can be variably weathered and fractured. The study area is located at the intersection between the PZ and the TZ and is therefore affected by at least two overlapping deformation events. The PZ in the southern part of Sweden is deformed to an NE–SW direction. A system of mafic dykes, northeast trending like PZ, has been highly deformed and metamorphosed to amphibolite grade rocks by the Sveconorwegian orogenic event. Locally, these dykes are severely weathered and altered to clay.

A second system of dykes, related to the TZ deformation, has its main trend to the northwest, parallel to the faults that create the horst–graben morphology. These diabase dykes are mainly

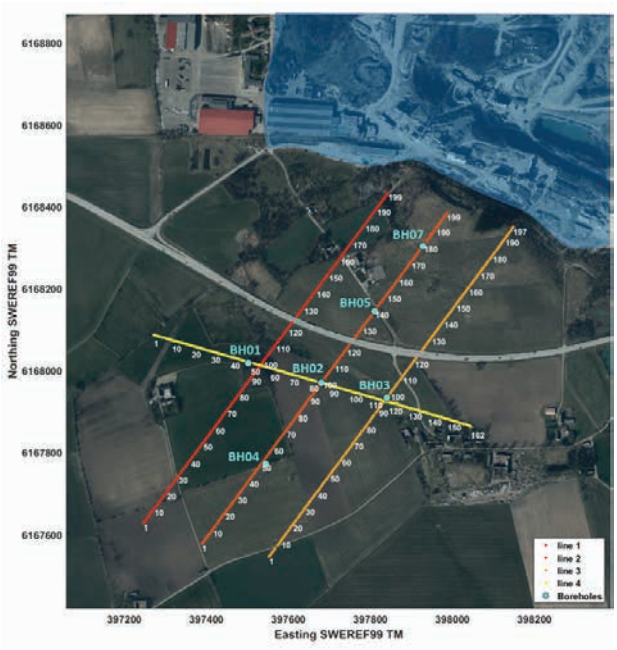

Figure 2 Location of the survey area (original orthophoto from Lantmäteriet 2015). Red to yellow lines represent the 2D layout of DCIP acquisitions. Light blue dots are the positions of the boreholes. The light blue shading marks out the location of the Dalby quarry.

sub-vertical and ca. 5–10 m thick. The basement rocks also show brittle deformation features that have been filled with mineralisation related to contact metamorphism and hydrothermal activities.

The bedrock is covered by glacial sediments (till) of a thickness of 5–25 m, here referred to as moraine deposit. The water table depth, measured in the available boreholes (Figure 2) during the year after the geophysical survey, is around 15–30 m, depending on the location and on the seasonal variation.

METHODOLOGY

The area of interest has been investigated by four 2D DCIP profiles (Figure 2): three parallel lines oriented SW–NE and a quasi-orthogonal line oriented WNW–ESE. Lines 1 and 2 are 1005 m long with 199 electrodes; Line 3 is 995 m long with 197 electrodes; and Line 4 has 167 electrodes for a total length of 805 m. The electrode spacing is 5 m, with the exception of a few areas where it was not possible to install electrodes, i.e., the two-lane road crossing the first three profiles. To overcome the discontinuity of the road, a couple of horizontal drillings were performed to be able to pass beneath the road and link cables together. A layout with two separated and parallel multi-conductor cables has been used. The two parallel cables with 10-m spacing takeouts were laterally separated by about 1–1.5 m and shifted along the line of 5 m to obtain an electrode spacing of 5 m. By using this configuration, we obtain two separate current and potential circuits, which reduces capacitive coupling in long multi-core electrode cables (Dahlin and Leroux 2012).

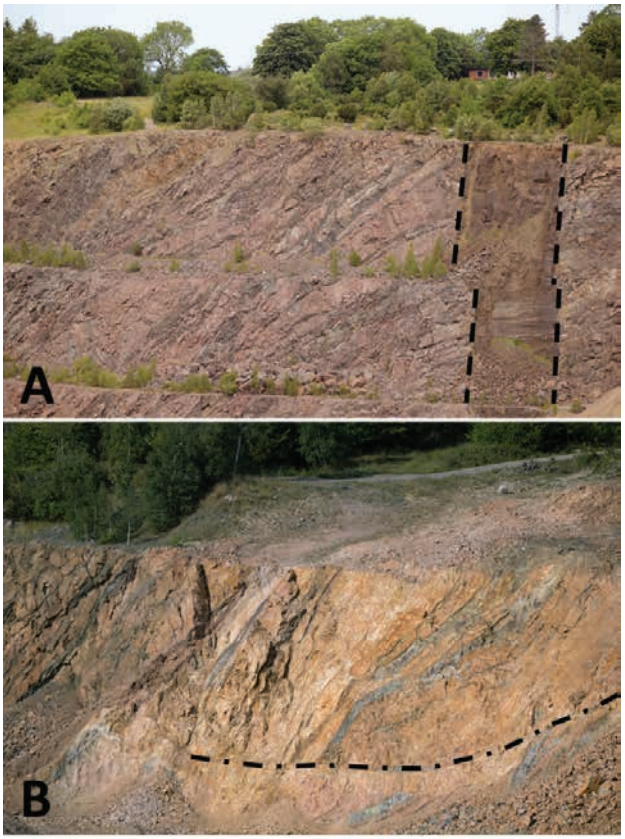

Figure 3 Examples of the crystalline bedrock from pictures taken at the Dalby Quarry. Gneiss is clearly visible in brown–red–grey colour, intensively pervaded by deformed amphibolite rocks, i.e., dark grey alignments dipping toward the left. In A, the black dashed lines mark the boundaries of a sub-vertical diabase dike, whereas in B, the dot-dashed black line highlights the presence of a brittle structure.

Data were collected with an ABEM Terrameter LS Instrument using a multiple-gradient nested array in a roll-along procedure to cover the entire length of the profiles. Each roll-along moved the lines 200 m further, with an overlapping section of 605 m with the previous acquisition. The gradient array protocol has parameter *s* in the range of 6 to 7 in the majority of the data and few added with larger *s*; whereas parameter *a* has the following values: 5, 10, 20, 40, 60, and 80 (Dahlin and Zhou 2006). Parameter *a* is the separation of the potential dipole as the number of electrodes between the measurement points, whereas parameter *s* is the distance of the current dipole, counted as a multiple of *a*.

The current injections are characterised by a 100% duty cycle, 4-second pulse length, and 3-cycle stacking waveform. Full waveforms for the transmitted current and the measured potentials were recorded at a sampling rate of 3750 Hz. The full-waveform recordings were processed as described by Olsson *et al.* (2016) to obtain reliable IP response information. This processing scheme is divided in four main steps, dealing separately with background drift, spikes, harmonic noise, and

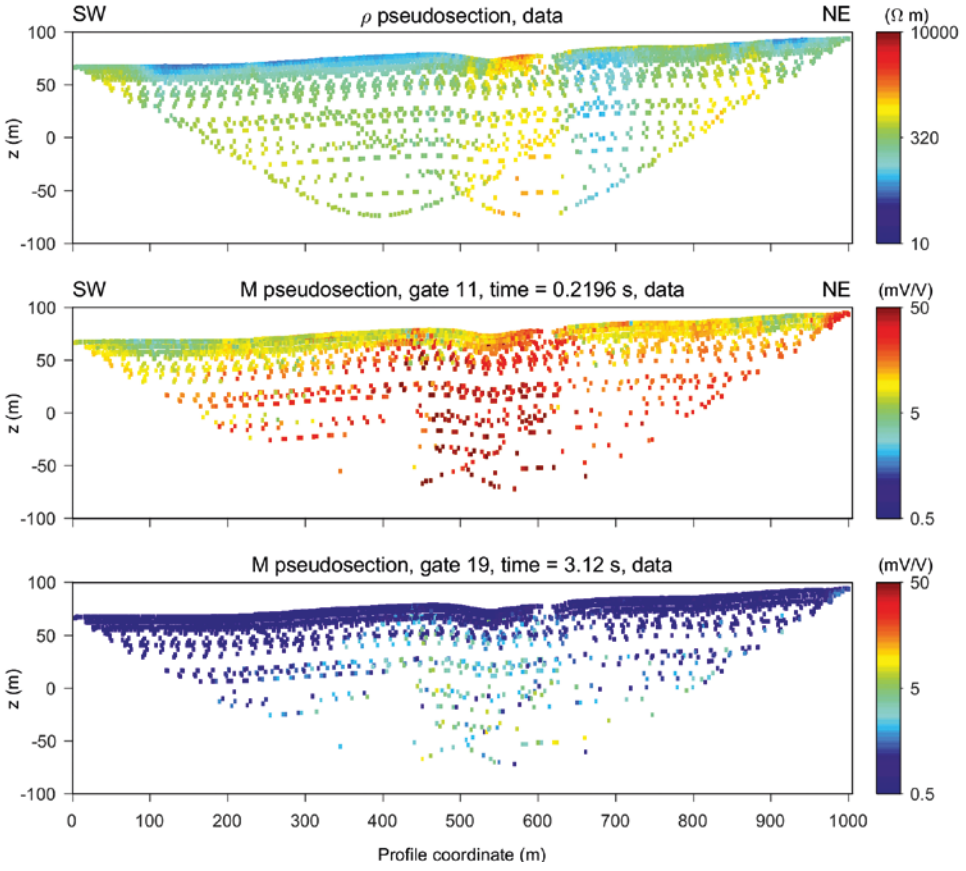

Figure 4 Example of pseudosections for Line 2: apparent resistivity data (on top) and apparent chargeability for two different time gates (at 219.6 and 3120 ms).

random noise. The first part of the processing scheme includes the removal of background potential drift. The drift is frequently present in full-waveform data as a shift of the measured electrical potentials over time, and it is mainly caused by ground self-potential and current-induced polarization of stainless-steel electrodes (Dahlin 2000). The drift often follows a Cole–Cole behaviour, and thus, this model is used for estimating and removing the background drift (Olssson *et al.* 2016). The second step involves filtering of potential spikes, usually seen in full-waveform data measured in rural environments with electrical fences for livestock management. The third processing step is the filtering of harmonic noise originating from household power supply lines (50 Hz in Sweden) and railway electrification system (16.67 Hz in Sweden), which can significantly mask part of the signal. The last step involves tapered gating of the waveform stacks into 24 time gates with logarithmically increasing gate widths, in the range from 1 to 3210 ms. This is necessary to obtain IP responses with a reduced number of samplings, starting from the full-waveform sampled at 3750 Hz, that cannot be used in the inversion procedure.

Further manual processing of resistivity and response curves was performed with the aim of removing the noisiest measurements or the noisiest time gates. The main part of the datasets shows responses from ground electromagnetic induction at earlier time gates of the response curves (from 1 to 7 ms), which can be regarded as noise when analysing IP signals. The final datasets contain between 3982 and 4045 quadripoles (89%–94% of the total amount of data), with the exception of the shorter Line 4 with 3241 quadripoles (97%). Figure 4 shows an example of a pseudosection of the raw data of Line 2 plotted as measured apparent resistivity values and apparent chargeability values of the same profile. The pseudosections show two of the 24 integrated time gates (at 219.6 and 3120 ms) to give a brief overview of the pre-processed IP response curves.

The 2D inversions (Figure 5) were carried out with the Aarhusinv software (Fiandaca *et al.* 2012) using a constant-phase angle (CPA) model (Binley *et al.* 2005), which assumes a constant phase of the complex resistivity for all frequencies. Model parameterisation is defined in terms of the DC resistivity and the phase of the complex conductivity (i.e., conductivity instead of resistivity, hence the phase is defined positive), as described in detail by Johansson, Fiandaca and Dahlin (2015). The standard deviation (STD) error of the apparent resistivity data was set to 1%, and the STD error for each IP time window was set to 10%; on top of this fixed STD error, a voltage-dependent error was added with a threshold of 0.1 mV (Olsson *et al.* 2015). The residual error of the final models, calculated as the chi statistical operator (χ), is 2.1±0.5. The simulated response curves assuming a CPA model fit the measured IP

responses with small residuals. We also inverted the data using a different model with a Cole–Cole parameterisation, retrieving similar data misfit, but decided to use the simplest model that can describe the shapes of the IP response curves, which is, in this case, the CPA model.

The depth-of-investigation (DOI) computation is based on a cumulative sensitivity approach that differs from the method proposed by Oldenburg and Li (1999). The actual method is built on an approximated covariance analysis applied to the model output from the inversion while considering the data STDs (Fiandaca *et al.* 2015). The 2D inverted section is subdivided in columns where the elements of the Jacobian are summed downwards for each parameter of the model as a function of depth, and the corresponding STD factor is computed. The DOI value is then defined by imposing a threshold value of the STD factor for each parameter and each column. A DOI threshold value of 2 means that the model below the DOI is resolved within a factor of two.

Seven percussion boreholes, with relative drilling logs to a depth of 175–250 m, are present at the site, located along the

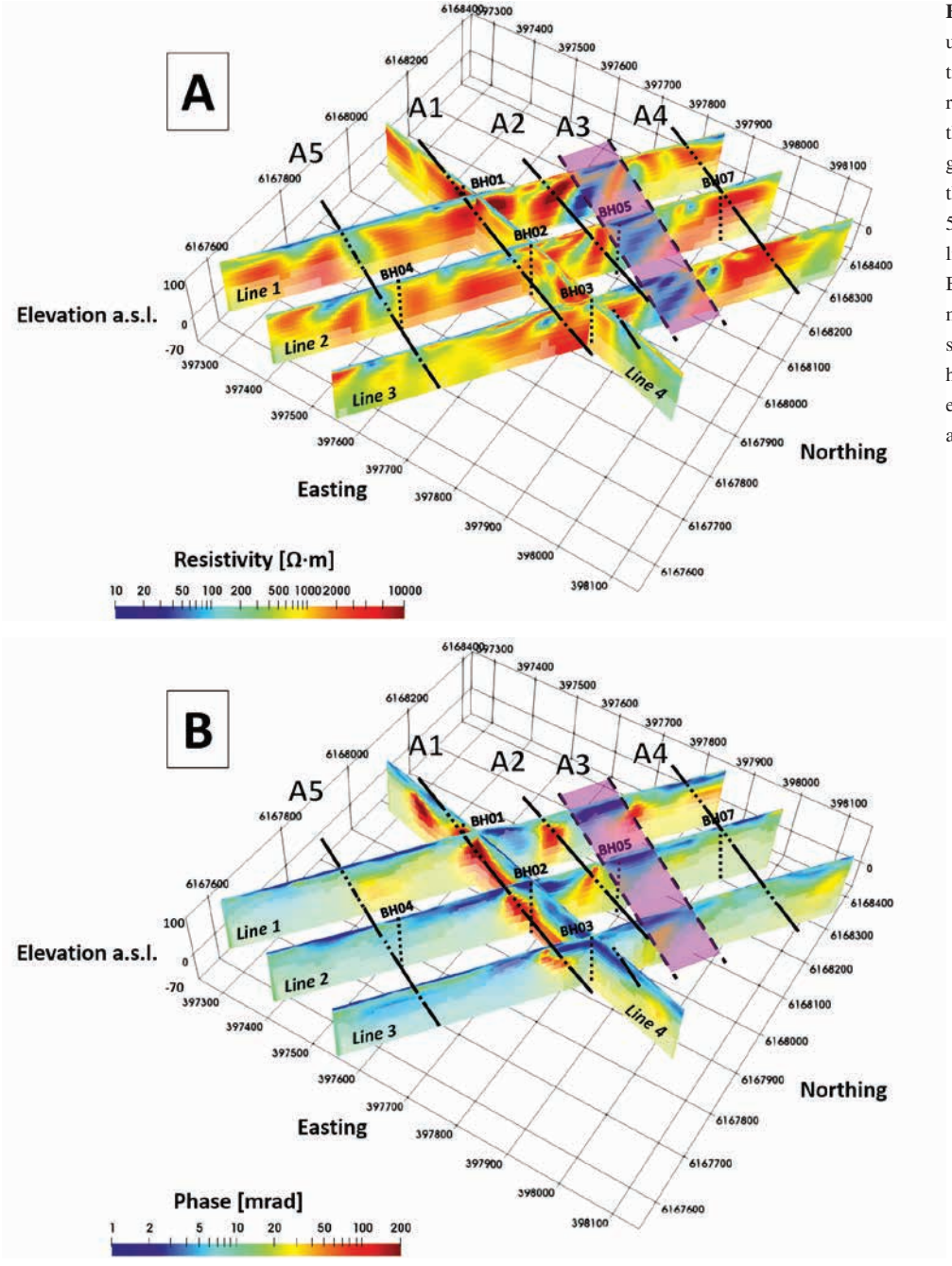

Figure 5 Three-dimensional visualisation of the inverted 2D sections. Figure A shows electrical resistivity imaging and Figure B the phase distribution. The light grey shadings represent the threshold of the DOI above 2 and 5 (respectively). Black dashed lines are the borehole positions. Black lines (A1, A2, A4, and A5) mark the presence of WNW–ESE structures. The purple area (A3) highlights a large anomaly in the electrical properties. Coordinates are Sweref99 TM (in metres).

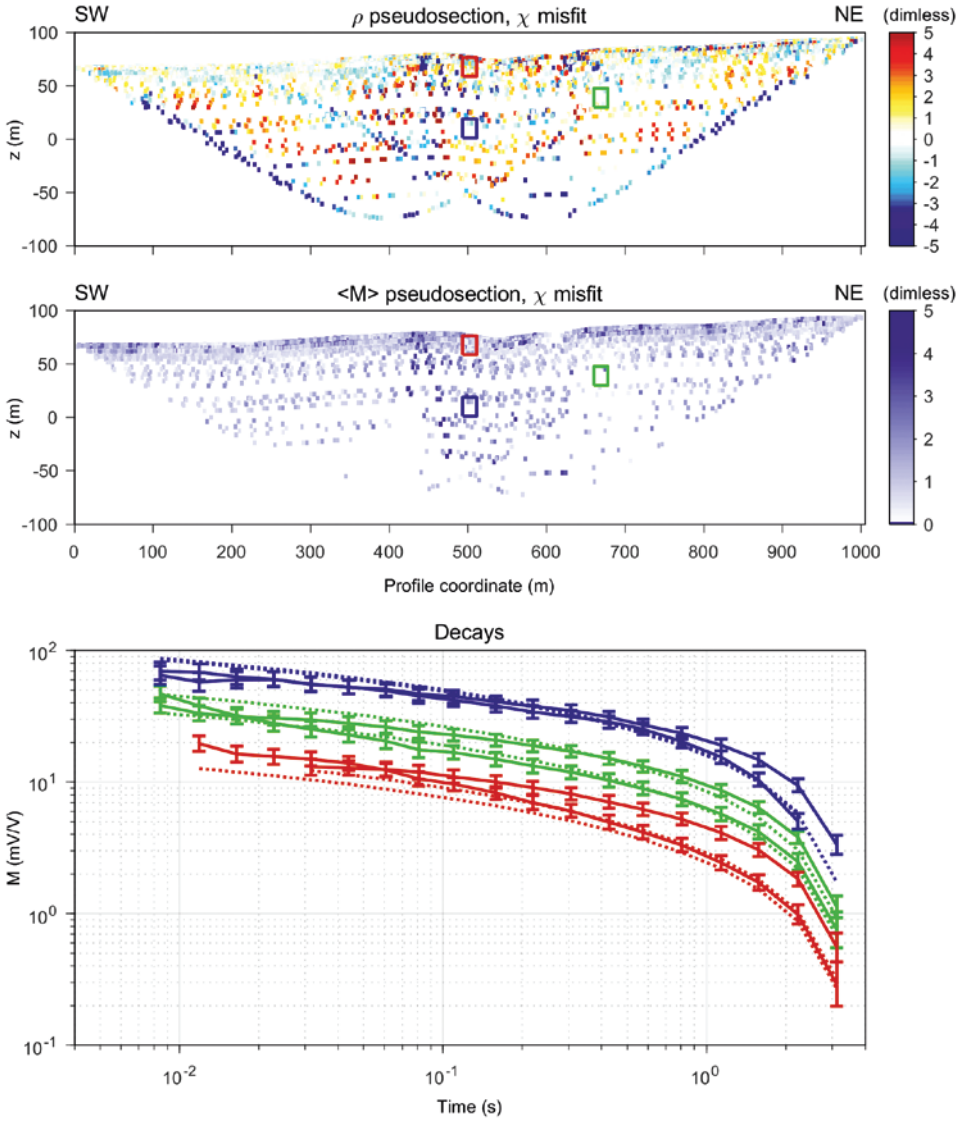

Figure 6 Example of chi misfit pseudosections for Line 2: (top) apparent resistivity and (middle) apparent chargeability. The apparent chargeability misfit is expressed in terms of summed absolute chi misfit for the full IP response. Examples of six response curves extracted from positions marked with rectangles are shown in the bottom figure; (solid lines) each different colour is the measured response after processing with STD for each gate; dashed lines are the corresponding forward models.

DCIP lines (Figure 2). The drillings took place several months after the geophysical survey; no boreholes with metal casing were present at the site during the DCIP acquisitions. The lithological description and the classification of alteration into five classes were visually estimated by the drilling company. Two boreholes, BH02 and BH05, were logged with DCIP measurements using a resistivity logging probe, i.e., a modified version of SASLOG 200, ABEM Instrument AB. As usual, the instrument acquires two standard borehole configurations, namely, short normal (SN) and long normal (LN). The modifications are the exclusion of the long lateral configuration, the addition of three different pole–dipole arrays, and the possibility to use four internal channels simultaneously to achieve time-efficient surveys. In the shallower portion of the boreholes, a metal casing has been used to prevent collapse of the sediments, and as a consequence, the logging survey has been conducted only in the deeper uncased part of the borehole.

RESULTS AND DISCUSSION

In Figure 5, the inverted DCIP profiles are plotted in a 3D view: Figure 5A represents the distribution of electrical resistivity (Ωm), whereas Figure 5B shows the phase of the complex conductivity of the CPA model (mrad). The shaded areas mask the lower reliability of the inverted electrical parameters, represented as thresholds of the DOI, fixed at 2 (low shading) and 5 (high shading). At lower values of the DOI (shallower part), the matching of the 2D profiles at the crossing points is quite consistent for both resistivity (ρ) and phase (ϕ). This aspect indicates limited 3D heterogeneity effect during the acquisition of the 2D profiles.

Figure 6 shows pseudosections of the chi misfit between modelled and measured apparent resistivity (top) and chargeability (middle) responses. In general, the apparent resistivity and chargeability misfits are low and evenly distributed throughout the pseudosection. However, at around 450 m, there

are slightly increased misfits for both parameters. In addition, for the lowest pseudo-depths in the apparent resistivity misfit, the misfit is mainly negative but still within a deviation of a few percentage. Figure 6 also shows examples of response curves and their corresponding forward responses for the inversion model (bottom). There is generally a good fit between measured and modelled IP responses for the CPA parameterisation. The fact that a CPA model matches the measured data is relevant knowledge: the same out-of-phase response can be assumed for a time window from 7 to 3000 ms. It is clear that not all the response curves can be fitted with the present model even if the majority of the measured responses can be described by a forward CPA model.

The inverted resistivity has a broad range of variation from about 10 to a maximum of about 20000 Ωm (Figure 5). The most resistive areas can be identified as fresh bedrock, i.e., with a limited degree of alteration and fractures, whereas the conductive portions are related to the quaternary fluvio-glacial sediments on top and anomalies in the crystalline basement. The inversion of IP signals shows clear and well-defined transitions in the phase angle values in a broad range (1–200 mrad).

The inverted sections show a complex and heterogeneous underground. The intricate distribution of the electrical properties can be easily justified by the local geology (Figure 3), where structures and fractures can have different mineral composition, water content, and degrees of weathering. In trying to summarise the heterogeneous image of the subsoil, it is possible to recognise a trend of aligned anomalies. The presence of quasi-parallel features, delineated by a distribution of electrical properties in the WNW–ESE direction, can be recognised. The different portions of subsoil, named as A1, A2, A3, A4, and A5, can be related to structures of the TZ as they are aligned in the same direction.

Principally for two reasons, the main features of the PZ that are oriented NE–SW in the study area, almost orthogonal to TZ, are not expected to be detected. The first is that Lines 1–2–3 are in the same direction of PZ structures and a single profile (Line 4) is not sufficient to detect orthogonal 2D structures. The second reason is related to the typology of PZ features, mainly of metamorphic origin with complex geometries at a metric scale, which are portrayed as almost homogeneous at the mean resolution of the DCIP profiles (decametric scale).

Comparisons between the lithological logs from drillings and the inverted DCIP profile are shown in Figures 8 to 10. Each Figure shows the electrical properties of a DCIP profile together with the lithological logs; hence, some of the borehole descriptions are repeated in the images. The 1D distributions of electrical properties (ρ and ϕ) are extracted from the DCIP inverted profiles, exactly where the boreholes are located. Two different values of DOI are plotted as horizontal lines, both for ρ and ϕ: solid line as low DOI with threshold 5 and dashed line as high DOI with threshold 2. The DOI may help in the comparison of the results, avoiding an over-interpretation in areas where the resolution of the inverted parameters is too low. A rough lithological description obtained from the percussion drillings is plotted together with an estimation of the degree of alteration in a qualitative scale from 1 to 5 (overlapping black dashed line). As the drillings have been performed with a percussion technique, the alteration index describes both weathering and pervasive fractures.

Table 1 summarises the values of the electrical quantities that characterise the different parallel lineaments, highlighted in Figure 5. A1 and A2 are characterised by high phase angles and high resistivity values; A3 and A5 are the opposite, defined by low IP and resistivity values; and A4 shows modest phase angles and high resistivity.

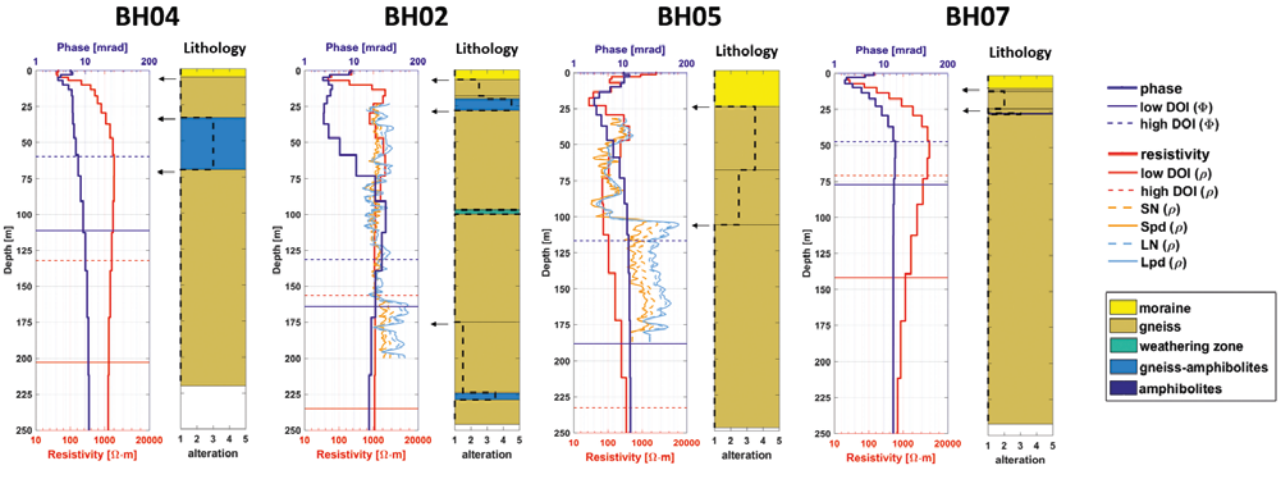

Figure 7 Borehole comparison for Line 2. Blue and red thick solid lines represent phase angle and resistivity, respectively, extracted as 1D profiles from 2D inverted DCIP tomography. Thin dashed and solid horizontal lines are the DOI depths for two different thresholds, i.e., 2 and 5, respectively. Orange and light blue lines (solid and dashed) are the results of the resistivity borehole logging. In the columns describing the lithology, a black dashed line shows the degree of alteration of the rock.

Subsoil lineament	Phase [mrad]	Resistivity [Ωm]	Possible interpretation
A1	> 50	> 2000	Amphibolite
A2	> 50	> 3000	Mafic dike?
A3	< 10	< 200	Fracture zone
A4	< 10	>2000	Fresh gneiss
A5	< 10	< 200	Fracture zone

Table 1 Summary of the mean electrical properties (ϕ and ρ) of the four parallel lineaments in Figure 5.

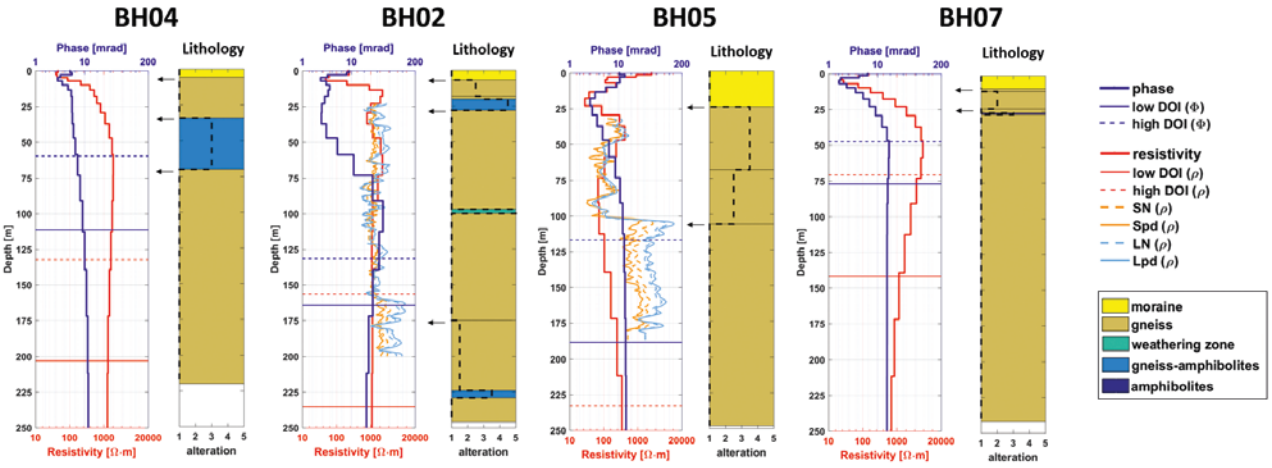

Figure 8 Borehole comparison for Line 3. See caption of Figure 7.

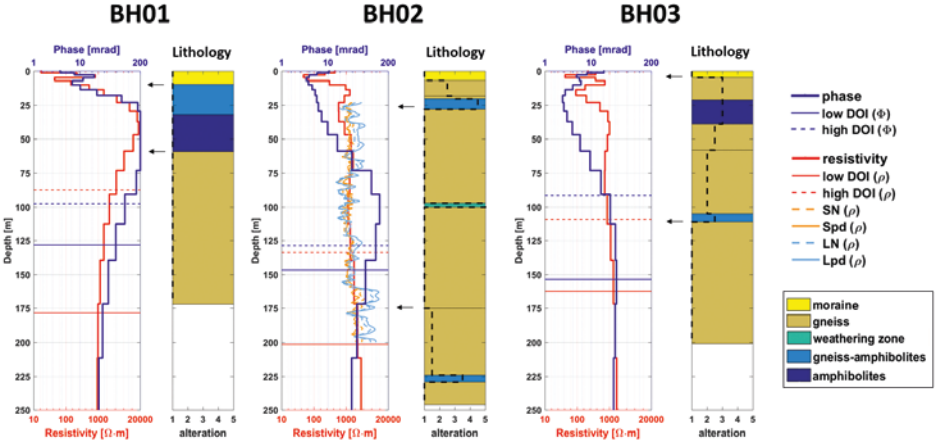

Figure 9 Borehole comparison for Line 4. See caption of Figure 7.

Anomaly A3 is characterised by a structure, i.e., 150–200 m broad from surface to the investigated depth, with deviant electrical properties: resistivity is lower than 200 Ωm and the IP response is restrained with a phase angle inferior to 10 mrad. Anomaly A5 is similar to A3 in character but narrower. The electrical properties of A3 and A5 may indicate weak zones in the bedrock. Some features linked to TZ tectonic activities, e.g., a fault or a fracture zone, may increase the secondary permeability of the basement, with the consequence of increased water content and larger specific surfaces prone to mineral alteration. An increase in clay minerals and of bulk moisture content reduces the electrical resistivity. The phase of the complex conductivity usually increases with rock alteration, except if a significant amount of interconnected clay minerals is acting as a conductor (Slater and Lesmes 2002). However, the phase can also be lowered by a larger degree of volumetric water content, as has been shown by laboratory experiments (e.g., Titov *et al.* 2004; Cassiani *et al.* 2009). Borehole BH05 has been drilled on the southern edge of A3, and the lithological log proves the presence of strongly weathered gneiss to a depth of 107 m from the topographic surface (Figure 7). Similarly, borehole BH04 has been drilled next to the northern edge of A5, and the lithological log proves the presence of strongly weathered gneiss–amphibolites from 34 to 70 m from the topographic surface (Figure 7).

The remaining linear features (A1, A2, and A4) are less univocal in the interpretation. A1 and A2 are characterised by an

alignment of IP features, with a phase higher than 50 mrad. These features may represent tectonic structures such as fractures filled by hydrothermal mineralisation that can increase the IP response or mafic dikes that contain polarizable minerals with a heterogeneous alteration, leading to a non-uniform resistivity distribution. In particular, A1 is a clear lineament of very high IP response (up to 200 mrad) that crosses BH01. The lithology of BH01 suggests that high resistivity and phase are due to a thick zone of amphibolite rocks (Figure 9), likely related to the inner curvature of a fold, where usually amphibolite migrates during metamorphic processes (see example in Figure 3). A4 is characterised by high resistivity that can be explained by resistive fresh gneiss with moderate IP response, as shown in the geological logging of borehole BH07 (Figure 7).

The sediment cover shows low values of ρ and ϕ, as it is expected for moraine deposits in this geological environment. Regarding the crystalline basement, the changes in resistivity are more likely correlated with the degree of weathering of the rock, marked out in Figures 7 to 9 with black arrows.

Two boreholes are located exactly at the crossing point between DCIP lines: BH02 for Lines 2 and Line 4; BH03 for Line 3 and Line 4. The values of the extracted electrical properties are not exactly the same even if they are mainly similar above the DOI. The discrepancy can be caused by some reduced 3D effect that is not taken into account in the 2D assumption of the inversion procedure. Nevertheless, even if the values are slightly different, the 1D profiles have the same shape and trend of variation.

The presence of amphibolite is documented in two boreholes, i.e., BH01 and BH03 (Figure 9). This geological feature is linked with a high phase angle for BH01, as aforementioned, whereas a very low IP response is recorded nearby BH03. This difference can be caused by a narrower amphibolite layer in BH03 (>20 m) than the layer of rock with mafic intrusions in BH01 (about 50 m). Moreover, BH03 shows a high degree of alteration (up to class 3) that can degrade the composition of mafic minerals.

Boreholes BH02 and BH05 were logged for a resistivity profile in the saturated zone: the dashed orange line is the SN configuration; the orange solid line is a pole–dipole array with 1-m spacing between potential electrodes (Spd); the light blue dashed line is the LN configuration; and the light blue solid line is a pole–dipole array with 5-m spacing between potential electrodes (Lpd). Larger logging arrays as LN and Ldp are consistent with the resistivity profiles from surface measurements above the DOI. In particular, Ln and Lpd acquisitions along BH02 show good agreement with both Line 2 (Figure 7) and Line 4 (Figure 9). In BH05, below 100-m depth, the logging configurations with a shorter spacing (SN and Spd) show lower ρ values. This deficiency is due to a poor penetration of these arrays into the rock mass, with the consequence that the fluid resistivity of the water-filled borehole dominates the response. Care must be taken in interpreting the results of resistivity loggings aimed at lithological and rock quality descriptions since the investigated volume of rock for each electrode configuration is not known. Furthermore, in BH05 below 100-m depth, there is a mismatch between resistivity from logging and surface measurements where the surface measurements strongly underestimate the resistivity. This is likely to be an effect of reduced resolution with depth from the surface measurements (not the case for DCIP logging).

IP signals cannot be directly linked to bedrock classification as the signal can be related to different unknown parameters of the geological materials. The phase of the complex conductivity is influenced by several parameters of the rock lithology, for example, pore space geometry (Weller and Slater 2015), presence of disseminated ores (Wong 1979), degree of saturation (Ulrich and Slater 2004), and salinity (Weller *et al.* 2011). An integrated interpretation of the IP results with electrical resistivity sections and drilling logs can facilitate the classification of the subsoil and the detection of lithological features. In this work, the combined interpretation of the electrical properties leads to the detection of quasi-parallel geological structures that follow the lineaments of the TZ tectonic zone. Moreover, a clear description of the crystalline basement in terms of mineralogy, tectonic structures, and rock alteration is obtained from the adjacent quarry (Figures 2 and 3); this constrains the interpretation of the geophysical results to some reliable geological features. It must be mentioned that BH01 on Line 4 (Figure 9) shows a relatively high phase angle, up to 200 mrad, coinciding exactly with layers rich in amphibolite that contain polarizable mafic minerals.

CONCLUSIONS

We have presented a case study where DCIP methodology has been performed on a large-scale survey with four 2D profiles that cover a planar space of about 1 km × 0.8 km. The goal was to map bedrock structures and material properties that are relevant from an engineering geological as well as environmental management perspective, by integrating electrical resistivity and IP data.

The results demonstrate that DCIP data can be successfully acquired and processed on a relatively large scale relevant for standard surveying for engineering and environmental applications. The majority of the acquired data are of sufficiently good quality to allow IP inversion despite the relatively large layouts and dipole spreads. The inverted geophysical parameters are consistent between the investigated lines for the electrical resistivity and the IP model sections. The variation of geophysical quantities is also consistent with borehole information, and the results show that DCIP surveys make a useful tool for mapping geological structures and specifically structural zones in the crystalline basement. The integration of IP models is a valuable tool for delineating geological structures that sometimes can be misinterpreted by using resistivity imaging only. In the case presented here, the main features related to TZ tectonic structures, trending WNW–ESE, are identified and classified according to weathering conditions and geophysical properties.

This kind of 3D geometries is often very difficult to recognise merely using drilling techniques, which must always be comple-

mentary to geophysical surveys. Possible weak zones related to regional geological settings can be mapped by the DCIP method. This knowledge provides a basis for adequate and appropriate design for constructions. Moreover, this information can suggest risk areas from a groundwater hydraulic point of view or can point out areas where further geotechnical and/or geophysical investigations need to be carried out.

ACKNOWLEDGEMENTS

Funding that made this work possible was provided by BeFo; Swedish Rock Engineering Research Foundation (ref. 314 and 331) and SBUF, The Development Fund of the Swedish Construction Industry (ref.12718 and 12719); and Formas, The Swedish Research Council for Environment, Agricultural Sciences and Spatial Planning (ref. 2012-1931), as part of the Geoinfra-TRUST framework (*http://www.trust-geoinfra.se/*). Furthermore, funding was provided by the Danish Council for Strategic Research as part of the GEOCON project (ref. 1305-00004B). The authors would like to specially thank Skanska for funding the field survey and allowing them to publish the results, especially Benjamin Andersson and Robert Sturk. Furthermore, they would like to thank Mathias Ronczka, Cécilie Finco, Elisabeth Lindvall, and Erik Warberg for their enthusiastic efforts in the field crew. The authors are also grateful to the team from SWECO, especially Bo Bergman and Mattis Johansson, for fruitful collaboration in connection with logistical organisation and providing reference data.

REFERENCES

Binley A., Slater L.D., Fukes M. and Cassiani G. 2005. Relationship between spectral induced polarisation and hydraulic properties of saturated and unsaturated sandstone. *Water Resources Research* **41**, W12417.

Brander L. and Söderlund U. 2009. Mesoproterozoic (1.47-1.44 Ga) orogenic magmatism in Fennoscandia; Baddeleyite U-Pb dating of a suite of massif-type anorhosite in S. Sweden. *International Journal of Earth Sciences* **98**, 499–516.

Cassiani G., Kemna A., Villa A. and Zimmermann E. 2009. Spectral induced polarization for the characterization of free-phase hydrocarbon contamination of sediments with low clay content. *Near Surface Geophysics* **7**(5–6), 547–562.

Cavinato G.P., Di Luzio E., Moscatelli M., Vallone R., Averardi M., Valente A. *et al.* 2006. The new Col di Tenda tunnel between Italy and France: integrated geological investigations and geophysical prospections for preliminary studies on the Italian side. *Engineering Geology* **88**(1), 90–109.

CEN. 2004. Basis of geotechnical design. In: *Eurocode 7: Geotechnical Design—Part 1: General Rules,* Section 2, pp. 19–37. London, UK: British Standards Institution.

Dahlin T. 2000. Short note on electrode charge-up effects in DC resistivity data acquisition using multi-electrode arrays. *Geophysical Prospecting* **48**, 181–187.

Dahlin T., Bjelm L. and Svensson C. 1999. Use of electrical imaging in site investigations for a railway tunnel through the Hallandsås Horst, Sweden. *Quarterly Journal of Engineering Geology and Hydrogeology* **32**(2), 163–173.

Dahlin T. and Zhou B. 2006. Multiple-gradient array measurements for multichannel 2D resistivity imaging. *Near Surface Geophysics* **4**(2), 113–123.

Dahlin T. and Leroux V. 2012. Improvement in time-domain induced polarization data quality with multi-electrode systems by separating current and potential cables. *Near Surface Geophysics*, 545–565.

Danielsen B.E. and Dahlin T. 2009. Comparison of geoelectrical imaging and tunnel documentation. *Engineering Geology* **107**, 118–129.

Fiandaca G., Ramm J., Binley A., Gazoty A., Christiansen A.V. and Auken E. 2012. Resolving spectral information from time domain induced polarization data through 2-D inversion. *Geophysical Journal International* **192**(2), 631–646.

Fiandaca G., Ramm J., Binley A., Gazoty A., Christiansen A.V. and Auken E. 2015. Depth of investigation for multi-parameters inversions. *Proceedings of the Near Surface Geoscience 2015*, 21st European Meeting of Environmental and Engineering Geophysics, Turin, Italy.

Ganerød G.V., Rønning J.S., Dalsegg E., Elvebakk H., Holmøy K., Nilsen B. *et al.* 2006. Comparison of geophysical methods for subsurface mapping of faults and fracture zones in a section of the Viggja road tunnel, Norway. *Bulletin of Engineering Geology and the Environment* **65**(3), 231–243.

Geisler T. and Schleicher H. 2000. Composition and U–Th-total Pb model ages of polygenetic zircons from the Vånga granite, south Sweden: an electron microprobe study. *Geologiska Föreningens i Stockholm Förhandlingar (GFF)* **122**, 227–235.

Högdahl K., Andersson U.B., Eklund O. (eds) *et al.* 2004. The Transscandinavian Igneous Belt (TIB) in Sweden: a review of its character and evolution. Special Paper 37. Espoo, Finland: Geological Survey of Finland.

Hubbard F.H. 1975. The Precambrian crystalline complex of southwestern Sweden. The geology and petrogenetic development of the Varberg Region. *Geologiska Föreningens i Stockholm Förhandlingar (GFF)* **97**, 223–236.

Johansson L., Lindh A. and Möller C. 1991. Late Sveconorwegian (Grenville) high-pressure granulite facies metamorphism in southwest Sweden. *Journal of Metamorphic Geology* **9**, 283–292.

Johansson S., Fiandaca G. and Dahlin T. 2015. Observed and conceptual influence of non-aqueous phase liquids on spectral induced polarization parameters. *Journal of Applied Geophysics* **123**, 295–309.

Klingspor I. 1976. Radiometric age-determinations of basalts, dolerites and related syenite in Skåne, southern Sweden. *Geologiska Föreningens i Stockholm Förhandlingar (GFF)* **98**, 195–216.

Lantmäteriet©. 2015. GSD-Ortophoto 1m raster resolution. *https://www.lantmateriet.se/*. Last access: December 2015.

Magnusson M.K., Fernlund J.M.R. and Dahlin T. 2010. Geoelectrical imaging in the interpretation of geological conditions affecting quarry operations. *Bulletin of Engineering Geology and the Environment* **69**(3), 465–486.

Marescot L., Monnet R. and Chapellier D. 2008. Resistivity and induced polarization surveys for slope instability studies in the Swiss Alps. *Engineering Geology* **98**(1–2), 18–28.

Möller A., O'Brien P.J., Kennedy A. and Kröner A. 2002. Polyphase zircon in ultrahigh-temperature granulites (Rogaland, SW Norway): constraints for Pb diffusion in Zircon. *Journal of Metamorphic Geology* **20**, 727–740.

Oldenburg D.W. and Li Y. 1999. Estimating depth of investigation in DC resistivity and IP surveys. *Geophysics* **64**, 403–416.

Olsson P.-I., Dahlin T., Fiandaca G. and Auken E. 2015. Measuring time domain spectral induced polarization in the on-time: decreasing the acquisition time and increasing the signal levels. *Journal of Applied Geophysics* **123**, 316–321.

Olsson P.-I., Fiandaca G., Juul Larsen J., Dahlin T. and Auken E. 2016. Doubling the spectrum of time-domain induced polarization by harmonic de-noising, drift correction, spike removal, tapered gating and

data uncertainty estimation. *Geophysical Journal International* **207**(2), 774–784.

Pelton W.H., Ward S.H., Hallof P.G., Sill W.R. and Nelson P.H. 1978. Mineral discrimination and removal of inductive coupling with multifrequency IP. *Geophysics* **43**(3), 588–609.

Rønning J.S., Ganerød G.V., Dalsegg E. and Reiser F. 2014. Resistivity mapping as a tool for identification and characterisation of weakness zones in crystalline bedrock: definition and testing of an interpretational model. *Bulletin of Engineering Geology and the Environment* **73**, 1225–1244.

Slater L.D. and Lesmes D. 2002. IP interpretation in environmental investigations. *Geophysics* **67**(1), 77–88.

Söderlund U. and Ask R. 2006. Mesoproterozoic bimodal magmatism along the Protogine Zone, S Sweden: three magmatic pulses at 1.56, 1.22 and 1.205 Ga, and regional implications. *Geologiska Föreningens i Stockholm Förhandlingar (GFF)* **128**(4), 303–310.

Söderlund U., Karlsson C., Johansson L. and Larsson K. 2008. The Kullaberg peninsula—a glimpse of the Proterozoic evolution of SW Fennoscandia. *Geologiska Föreningens i Stockholm Förhandlingar (GFF)* **130**(1), 1–10.

Storz H., Storz W. and Jacobs F. 2000. Electrical resistivity tomography to investigate geological structures of the earth's upper crust. *Geophysical Prospecting* **48**, 455–471.

Titov K., Kemna A., Tarasov A. and Vereecken H. 2004. Induced polarization of unsaturated sands determined through time domain measurements. *Vadose Zone Journal* **3**, 1160–1168.

Ulrich C. and Slater L. 2004. Induced polarization measurements on unsaturated, unconsolidated sands. *Geophysics* **69**(3), 762–771.

Wahlgren C.-H., Cruden A.R. and Stephens M.B. 1994. Kinematics of a major fan-like structure in the eastern part of the Sveconorwegianorogen, Baltic Shield, south-central Sweden. *Precambrian Research* **70**, 67–91.

Weller A., Breede K., Slater L. and Nordsiek S. 2011. Effect of changing water salinity on complex conductivity spectra of sandstones. *Geophysics* **76**(5), F315–F327.

Weller A. and Slater L. 2015. Induced polarization dependence on pore space geometry: Empirical observations and mechanistic predictions. *Journal of Applied Geophysics* **123**, 310–315.

Wong J. 1979. An electrochemical model of the induced-polarization phenomenon in disseminated sulfide ores. *Geophysics* **44**(7), 1245–1265.